Applied Physics Letters ARTICLE pubs.aip.org/aip/apl

Capacitance characterization and current transport mechanism of $ZnSnN_2$ heterojunctions

Cite as: Appl. Phys. Lett. **125**, 242102 (2024); doi: 10.1063/5.0241401
Submitted: 30 September 2024 · Accepted: 26 November 2024 ·
Published Online: 10 December 2024

View Online Export Citation CrossMark

Fan Ye,[a] Zi-Cheng Zhao, Cang-Shuang He, Jian-Lin Liang, Qian Gao, Yi-Zhu Xie, Dong-Ping Zhang, and Xing-Min Cai[a]

AFFILIATIONS

Key Laboratory of Optoelectronic Devices and Systems of Ministry of Education and Guangdong Province, Shenzhen Key Laboratory of Advanced Thin Films and Applications, College of Physics and Optoelectronic Engineering, and State Key Laboratory of Radio Frequency Heterogeneous Integration, Shenzhen University, Shenzhen 518060, China

[a]Authors to whom correspondence should be addressed: yefan@szu.edu.cn and caixm@szu.edu.cn

ABSTRACT

The trap and defect energy levels of $ZnSnN_2$ and the current transport mechanism of its heterojunctions are studied. A shallow energy level at 105 meV below the conduction band minimum (E_c) of $ZnSnN_2$ is detected and its possible origin is the intrinsic antisite defect of Sn_{Zn} (Sn occupy the position of Zn in $ZnSnN_2$), besides the traps located at 0.67, 1.03 and 1.06 to 1.21 eV below E_c. The interface states of $ZnSnN_2$ heterojunctions form two discrete energy levels with one at $E_c + 0.05$ eV and another at $E_c - 0.03$ eV. The current of $ZnSnN_2$ heterojunctions is controlled by thermionic emission at relatively low bias voltage and limited by space charge at higher bias voltage. The barrier height of the heterojunctions is inhomogeneous, which obeys Gaussian distribution and possibly results from interface roughness.

Published under an exclusive license by AIP Publishing. https://doi.org/10.1063/5.0241401

14 December 2024 12:01:40

Developing solar cells based on Earth-abundant and eco-friendly semiconductors is essential in reducing the cost and expanding the application of photovoltaic (PV) technology.[1–7] $ZnSnN_2$ is considered as an eco-friendly solar cell absorber material that can meet terawatt-level energy demands at low cost.[4–6,8–21] Its advantages include a direct bandgap, high absorption coefficient ($\sim 10^5\,cm^{-1}$), Earth-abundance of elements, non-toxicity of both the elements and the compound, and low cost. It belongs to the Zn-IV-N_2 (IV = Si, Ge, and Sn) family whose bandgap can match the solar spectrum.[10–13] $ZnSnN_2$ is also considered highly competent in photocatalytic and light emission device applications.[22,23]

Theoretical work shows that $ZnSnN_2$ is n-type conductive with electron density of $10^{19}\,cm^{-3}$ or even higher and with antisite defect of Sn_{Zn} (Sn occupying the position of Zn) as the major donor.[4,5] In experiments, its electron density has been reduced[11,24–28] to around or below $10^{16}\,cm^{-3}$. Devices of $ZnSnN_2$, including heterojunctions (HJ), HJ solar cells, Schottky diode, and Schottky barrier solar cells, have been studied.[6,29–32]

However, much still remains unknown about $ZnSnN_2$ and its devices. The energy levels of defects and traps in $ZnSnN_2$ and the current transport mechanism of its HJ have not been studied. In this paper, $ZnSnN_2$ HJ, with Cu_2O[7,33–37] as the p-type layer, is prepared with sputtering. The properties of $ZnSnN_2$ and the HJ are studied. The defects and traps in $ZnSnN_2$ as well as the interface states and current transport mechanism of the HJ are revealed.

Both $ZnSnN_2$ and Cu_2O were prepared with magnetron sputtering. The base pressure of the vacuum chamber was 5.0×10^{-4} Pa. To measure the properties of $ZnSnN_2$ and Cu_2O, the substrates used were K9 glass and Si, which were ultrasonically cleaned in acetone, ethanol, and de-ionized water with the cleaning lasting for 15 min in each liquid. The rotational speed of the substrate holder was 0.6π rad/s. Before film deposition, the target was sputtered for 5 min to clean the target surface. An alloy target of Zn and Sn (99.999%) was used to deposit $ZnSnN_2$ and the atomic ratio of Zn to Sn is 6:1. Argon gas (99.99%) and nitrogen gas (99.999%) were introduced into the chamber. The flowrate of argon was eight standard cubic centimeters per minute (sccm) and that of nitrogen was 5 sccm. The working pressure was 5 Pa and the substrate temperature was 100 °C. Radio frequency (RF) sputtering was used and the power was 30 W. The deposition time was 4 h. A circular Cu plate (99.999%) was used as the target to deposit Cu_2O with direct current (DC) sputtering. The gases were Ar (99.99%) with a flow rate of 30 sccm and O_2 (99.999%) with a flow rate of 4 sccm. The working pressure was 0.6 Pa, the substrate temperature was 400 °C, and the deposition time was 1 h. The DC power was 50 W.

The fabrication of Cu_2O\$ZnSnN_2$ pn HJ (glass\ITO\$Cu_2O$\$ZnSnN_2$\InSn) and the characterization methods of $ZnSnN_2$

Published under an exclusive license by AIP Publishing

and Cu_2O and the PV properties of the HJ are elaborated in the supplementary material. In forward bias, Cu_2O was connected to the positive electrode of the power source. The room temperature (RT) capacitance C vs voltage V (CV) curves of the devices at different frequencies were measured with an instrument (Victor, VC4092E LCR) equipped with a cryogenic platform (JANIS). The DC bias was from −1.00 to 1.00 V and the alternative current (AC) excitation source was 30 mV. The drive level capacitance profile (DLCP) and admittance spectroscopy (AS) curves were also measured with the same instrument. For RT DLCP measurements, the DC bias was from −0.25 to 0 V, the AC amplitude was from 0.015 to 0.135 V while the frequency was the same as that used for the RT CV curves. The zero-bias AS curves were measured from 180 to 380 K and the frequency was from 100 Hz to 1 MHz.

The dark temperature dependent IV or JV (I is the current and J is the current density) curves of the HJ were measured using a source measure unit instrument (Keithley 4200-SCS) and the temperature of the HJ was controlled by a constant temperature heating system (JF-956S, JFTOOLS, China).

The characterization results of $ZnSnN_2$ and Cu_2O and the PV properties of the HJ are presented in Figs. S1–S3 of the supplementary material. Figure 1(a) shows the RT CV curves measured at different frequencies, f. These CV curves are equivalent to metal/n-type semiconductor Schottky junctions.[38] Besides series resistance, the reverse-biased HJ capacitance C also results from those induced by interface states (C_{IS}), interface layer (C_{IL}), and space charge (C_{SC}). C_{SC} equals $A_{sc}/(V_{bi}-V)^{1/2}$ where A_{sc} is a constant, V_{bi} is the built-in potential of the junction, and V is the applied voltage. The measured C here decreases with increasing frequency, mainly due to the decrease in response of the interface states with increasing frequency. In the reverse-biased region, C is equivalent to C_{IL} in series with two parallel branches, one is C_{SC} and another is C_{IS}:[38] C^{-1} equals $C_{IL}^{-1} + (C_{SC} + C_{IS})^{-1}$. If the interface layer is thin enough, C_{IL}^{-1} is negligible and so

$$C = C_{SC} + C_{IS} = A_{SC}/(V_{bi} - V)^{1/2} + C_{IS}. \tag{1}$$

The C^{-2} vs V curves are shown in Fig. S4 of the supplementary material, and it can be seen that they are not linear, implying that C_{IS} cannot be ignored.

With A_{sc}, V_{bi}, and C_{IS} as the fitting parameters, all the CV curves are fitted to Eq. (1) and the fitting results are presented in Table S1 of the supplementary material (the curves obtained at 900 and 500 Hz cannot be fitted and will be analyzed later). The successful fitting implies that the interfacial layer is thin enough and so C_{IL} can be ignored. A_{sc} and C_{IS} are found to decrease while V_{bi} increases with increase in frequency, in agreement with other results.[39] The fitted C_{SC}^{-2} or $(C–C_{IS})^{-2}$ vs V curves are shown in Fig. 1(b). After C_{IS} is removed, the C_{SC}^{-2} vs V curves become linear for 1, 0.9, and 0.5 MHz due to the fact that deep levels respond less at higher frequencies. From the curve at 1 MHz, the built-in potential V_{bi} is 0.59 V and the barrier height φ_b is calculated to be 0.67 V since the gap between the conduction band minimum E_c and the Fermi level E_f of $ZnSnN_2$ is 0.08 eV (see the supplementary material). The C_{SC}^{-2} vs V curves at 100–9 kHz are still slightly curved (Fig. S5), implying the effect of deep levels or traps. The energy position and density of these deep levels are calculated[39–41] and listed in Table S2 of the supplementary material. Traps at 1.21, 1.14, and 1.09 eV below E_c are found. Deep energy levels can deteriorate the performance of solar cells by trapping carriers to reduce short circuit current.

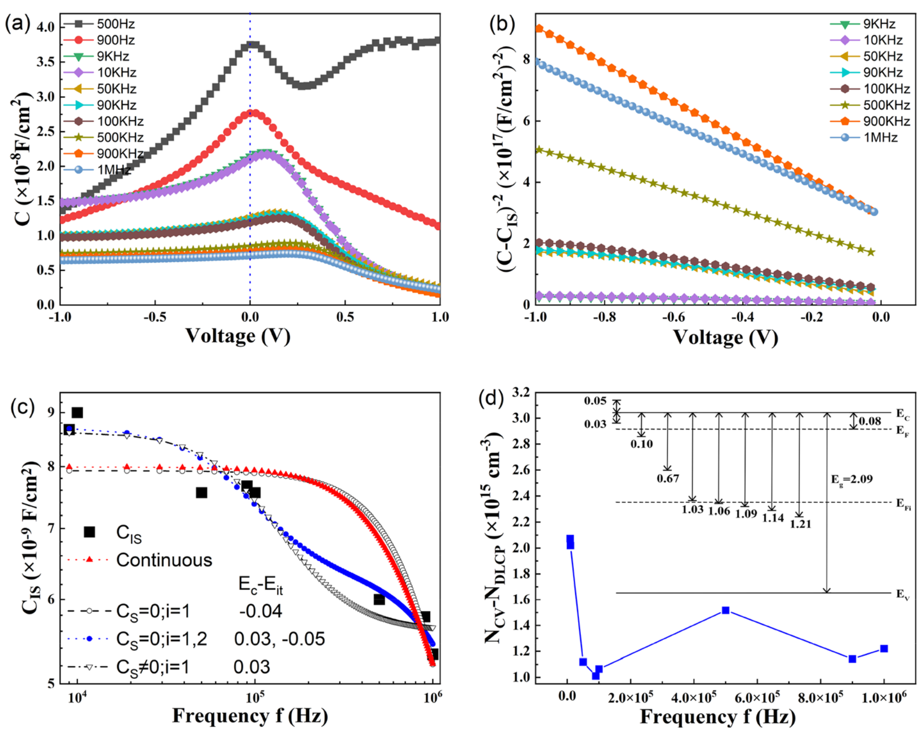

FIG. 1. (a) CV curves; (b) C_{SC}^{-2} or $(C - C_{IS})^{-2}$ vs V curves; (c) C_{IS} vs f data and the theoretical fitting; (d) N_{it} vs f [Inset: the energy levels of interface states and defects or traps, the unit is eV; the bandgap energy of $ZnSnN_2$ is from Fig. S1(e), supplementary material].

14 December 2024 12:01:40

Published under an exclusive license by AIP Publishing

The fitted C_{IS} data with four fitting models are shown in Fig. 1(c). For interface states forming continuous energy levels, C_{IS} equals $q^2 D_{it}(\omega\tau)^{-1} arctg(\omega\tau)$, where q is the unit charge, D_{it} and τ are the density and time constant of interface states, ω is the angular frequency (ω equals $2\pi f$).[42] A fitting to this model shows that D_{it} and τ are 4.99×10^{10} states $\cdot$ eV^{-1} $\cdot$ cm^{-2} and 2.40×10^{-7} s. However, the overlap between C_{IS} and the fitting curve is poor, possibly implying this model fails here. For interface states forming discrete levels, C_{IS}[42] is expressed as follows:

$$C_{IS} = C_S + \sum\nolimits_1^m C_{it-i}/[1 + (2\pi f \tau_i)^2], \tag{2}$$

where C_S is the semiconductor capacitance, m is the total number of discrete levels, *i* labels the *i*th level, τ_i and $C_{it\text{-}i}$ are the time constant and the capacitance of the *i*th level. With $C_S = 0$, the fitting results show that the curve with two discrete levels overlaps with the C_{IS}-f data much better than that with one level. If C_S is used as a fitting parameter, only the model of m = 1 works. The fitting results are listed in Table S3 of the supplementary material. The density of interface states $D_{it\text{-}i}$ and the corresponding interface states $E_{it\text{-}i}$ are also calculated and listed in Table S3 since $D_{it\text{-}i}$ equals $C_{it\text{-}i}/q^2$ while

$$\tau_i = f_i^{-1} = [v_{th}\sigma_n N_c]^{-1} \exp[(E_c - E_{it-i})/(kT)], \tag{3}$$

where f_i is the *i*th level frequency, v_{th} is the thermal velocity of electrons, σ_n is the capture cross section, N_c is the density of states [$v_{th}\sigma_n N_c$ equals 2.10×10^6 Hz as shown later; for n-type semiconductors, the measurement frequency is too high for holes to follow and so the interface states detected are around the conduction band but not the valence band in Eq. (3)].[42] From the model with $C_S = 0$ and m = 2, E_c-$E_{it\text{-}1}$ = 0.03 eV and this agrees with that obtained from $C_S \neq 0$ and m = 1. The model with $C_S = 0$ and m = 2 also shows that another energy level is 0.05 eV above E_c. This energy level needs further work though energy levels of impurities,[43] defects,[44] or interface states[45] above E_c are found in other semiconductors. Interface states are also harmful since they lead to interface recombination, which reduces the open circuit voltage.

The CV curves at 900 and 500 Hz cannot be fitted to Eq. (1) and the corresponding C^{-2}–V curves are shown in Fig. S6 of the supplementary material. These C^{-2}–V curves show concave-up curvature and can be divided into three linear sections due to interface states and deep levels. If we suppose that the interface states are in equilibrium with $ZnSnN_2$, N_D and V_{bi} of the first section can be calculated from the slope and horizontal intercept of section 1, while from section 2 and 3 the energy levels and the density of traps can be calculated (Fig. S6).[46,47] From the curve measured at 500 Hz, two trap energy levels at E_c-E_{DL} = 0.67 and 1.03 eV are found, while from that at 900 Hz E_c-E_{DL} = 0.67 and 1.06 eV are obtained. The deep energy levels and interface states are shown in the inset of Fig. 1(d).

From the CV curves, the depth profile of charge density, N_{CV}, which results from free carrier density as well as bulk and interfacial defect density can be obtained, while from drive level capacitance (DLC) the depth profile of the charge density, N_{DLCP}, which only results from the former two, can be obtained (Fig. S7 of the supplementary material).[48] The zero-bias difference between N_{CV} and N_{DLCP} at each frequency is exactly the total interface defect density N_{it} and is shown in Fig. 1(d). N_{it} varies with the frequency and is found to be around 1.5×10^{15} cm^{-3}. The possible peak at 0.5 MHz implies the interface states energy level is 0.04 eV below E_c according to Eq. (3), roughly in agreement with Fig. 1(c). Below 90 KHz, N_{it} increases with a decrease in f in the measurement range. If we suppose that the minimum measurement frequency of 9 KHz is just the peak of N_{it}, the corresponding energy level of the interface states will be 0.14 eV below E_c according to Eq. (3). If the N_{it} peak is below 9 KHz, the corresponding energy level will be much deeper than 0.14 eV.

Figure 2(a) shows the capacitance C vs f obtained from AS. A step is seen in the curves and this suggests a discrete defect level is detected.[6,49] To obtain the activation energy E_a of this defect, the $-\omega dC/d\omega$ vs ω curves at each temperature are calculated, and from these curves, the angular frequency ω_0 corresponding to the maximum of the curve can be obtained. The relation between ω_0 and the activation energy E_a is that ω_0 equals $2\pi\nu_0 T^2 \exp[-E_a/(kT)]$ or $2\pi f_0$, where υ_0 is the pre-exponential factor independent of temperature. Figure 2(b) shows the ω_0/T^2 vs 1000/T curve. υ_0 is calculated to be 23.34 Hz/K^2 and so $v_{th}\sigma_n N_c$ equals 2.10×10^6 Hz according to Eq. (3). E_a is found to be 105 meV (or 0.10 eV). The integrated total density based on Gaussian distribution, N_t, is 1.66×10^{16} cm^{-3} [Fig. 2(c)].

There are three possible origins for this energy level: from Cu_2O, the interface states, or $ZnSnN_2$. It is known that the preparation methods have an influence on E_a of defects. In Ref. 35, the E_a values for Cu_2O deposited at 600 and 1070 K are 0.23 and 0.19 eV. The preparation methods of our Cu_2O are very similar to that except that the substrate temperature used is 673 K here. The E_a of Cu_2O here should be between 0.23 and 0.19 eV, larger than 105 meV. This level also cannot result from interface states since the energy levels of interface states are at E_c−0.03 eV or E_c+0.05 eV in Fig. 1(c) while one around E_c−0.04 eV and another deeper than E_c−0.14 eV are estimated in Fig. 1(d). Therefore, this level can only come from $ZnSnN_2$ and the possible origin is the antisite defect of Sn_{Zn} since in $ZnSnN_2$, Sn_{Zn} is the major donor having the lowest formation energy.

Figure 2(d) shows the experimental and fitted Nyquist spectra of the HJ and the inset shows the equivalent circuit used for fitting.[6] The HJ can be fitted with one resistance R_s in series with two parallel branches: one is the parallel resistance R_p and another is the constant phase element (CPE, which includes two parameters: CPE-P and CPE-T—CPE-P is within 0–1, CPE-P = 1 implies that it is a pure capacitor while CPE-P = 0 implies it is a pure resistance). The fitted R_s, R_p, CPE-P, and CPE-T are 30.18 Ω, 3199 Ω, 0.81, and 1.24×10^{-8}, respectively. The time constant of the CPE, which equals $[R_p \times (CPE - T)]^{1/(CPE-P)}$, is calculated to be 3.97×10^{-6} s. This is larger than that of the interface states (Table S3), suggesting that interface states have a weak influence on the current transport. The existence of CPE also implies interface roughness.

The dark JV curves at different temperatures are shown in Fig. 3(a). As the temperature increases, J increases. In the forward double log JV curves [Fig. 3(b)], the slope of the curves at lower bias (<1 V) is close to 1, indicating Ohmic conduction and the current is controlled by the junction while the slope approaches 2 under high bias voltage, indicating that space charge limited current (SCLC) gradually becomes dominant.

The possible transport models of HJ[50–53] currents include tunneling, diffusion, generation/recombination in the space charge region, and thermionic emission (TE). In these models, the forward bias current density J equals $J_s\{\exp[A(T)V]-1\}$, where J_s is the saturation

14 December 2024 12:01:40

Published under an exclusive license by AIP Publishing

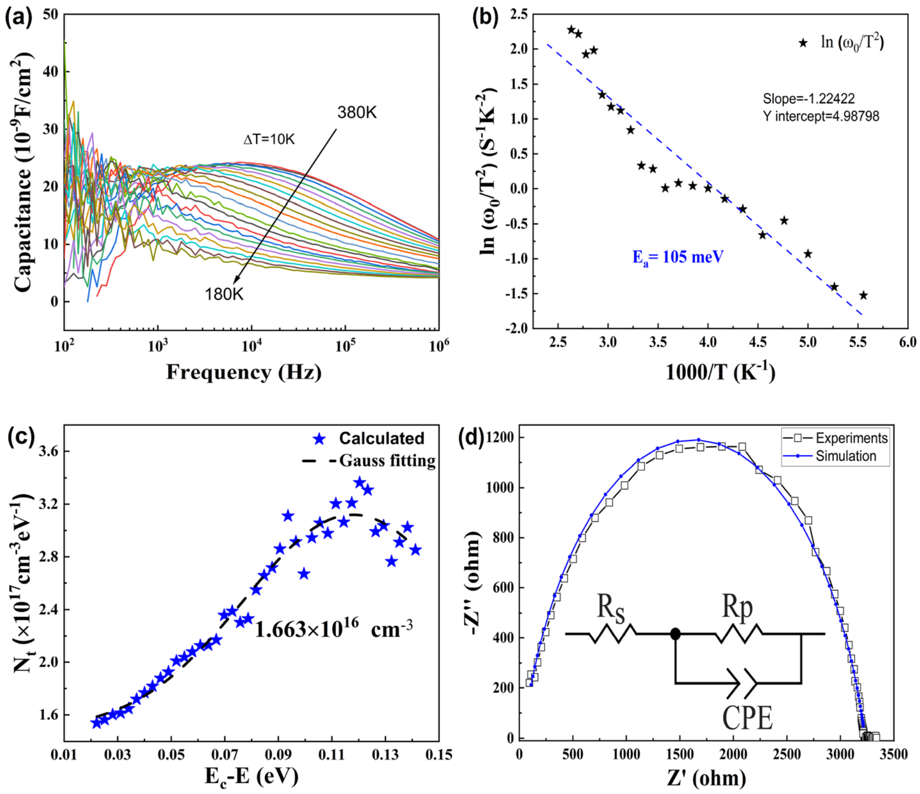

FIG. 2. (a) The admittance spectra of the HJ. (b) The Arrhenius plot of ln(ω_0/T^2) vs 1000/T. (c) The integrated density of the defect or trap. (d) The impedance spectrum of the HJ.

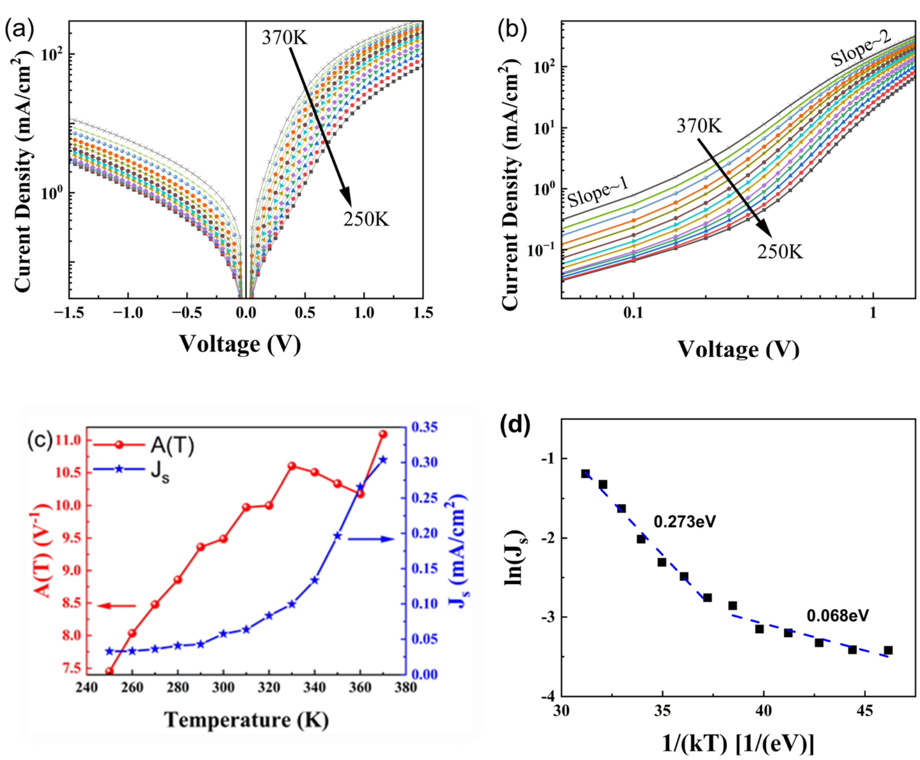

FIG. 3. (a) J∼V curves at 250–370 K. (b) Forward bias logarithmic J∼ logarithmic V curves. (c) A(T) and J_s vs T. (d) ln (J_s) vs 1/(kT).

14 December 2024 12:01:40

Published under an exclusive license by AIP Publishing

current density, A(T) is the exponential factor. When the applied voltage is over 3kT/q, J just equals $J_s\exp[A(T)V]$. J_s and A(T) can then be obtained from the linear region of the lnJ vs V plot, as shown in Fig. 3(c). It is seen that A(T) is not a constant in the whole temperature range and this excludes the possibility of tunneling. In addition, if the current is due to diffusion or generation/recombination in the space charge region, the activation energy from the $\ln J_s$ vs 1/(kT) curve would be the bandgap or half the bandgap. However, the activation energy from the $\ln J_s$ vs 1/(kT) curves is just about 0.273/0.068 eV [Fig. 3(d)], far smaller than that of Cu_2O or $ZnSnN_2$. Therefore, the current at low bias is controlled by TE.

According to the TE model, the JV relation is given by

$$J = J_s\{\exp[q(V - JR_s)/(nkT)] - 1\} + J_{sh}, \quad (4)$$

where

$$J_s = A^{**}T^2\exp(-q\varphi_b/kT). \quad (5)$$

J_{sh} equals $(V\text{-}IR_s)/R_{sh}$, R_s is the resistance in series with the diode, R_{sh} is a resistance in parallel to R_s and the diode, A^{**} is the effective Richardson coefficient [A^{**} of $ZnSnN_2$ is 14.40 (Ref. 29) $A\cdot cm^{-2}\cdot K^{-2}$], n is the ideality factor, φ_b is the barrier height, and the other symbols are consistent with the previous equations. With φ_b, n, R_s, and R_{sh} as the fitting parameters, the current density in the junction-controlled region (below 1 V) can be fitted to Eq. (4) and the fitting results are presented in Figs. 4(a) and 4(b). The barrier height φ_b increases with temperature increase while the ideality factor n is over 1 and decreases with temperature increase, implying barrier height inhomogeneity (BHI).[54–56] The series resistance R_s decreases with temperature decrease due to carrier freezing-out while R_{sh} increases with temperature increase.[50]

From Eq. (5), the following equation can be obtained:

$$\ln(J_s/T^2) = \ln(A^{**}) - q\varphi_b/(kT). \quad (6)$$

Equation (6) shows that $\ln(J_s/T^2)$ vs q/(kT) curves (the Richardson plot) will be linear. In the Richardson plot in Fig. 4(c), the linearity in the whole temperature range is not good. φ_b and A^{**} are 0.12/0.26 V and $3.69\times10^{-8}/1.28\times10^{-5}$ $A\cdot cm^{-2}\cdot K^{-2}$ in the low/high temperature range. The obtained A^{**} is much smaller than the theoretical value, also suggesting possible BHI.[54–56] With the presence of BHI, the relations between φ_b, n, and T are as follows:[54,55]

$$\varphi_b = \overline{\varphi_{b0}} - q\sigma_0^2/(2kT), \quad (7)$$

$$n^{-1} - 1 = -\rho_2 + q\rho_3/(2kT), \quad (8)$$

where $\overline{\varphi_{b0}}$ and σ_0 are standard barrier height and deviation at zero-bias while ρ_2 and ρ_3 are two coefficients. Figure 4(d) shows the plots of φ_b and n^{-1}–1 vs q/(2kT). From Eq. (7), $\overline{\varphi_{b0}}$ and σ_0 are obtained to be 1.05 and 0.15 V while from Eq. (8), ρ_2 and ρ_3 are 0.44 and −0.01 V. Since φ_b is related to temperature according to Eq. (7), Eq. (6) can now be turned into the modified Richardson relationship given by

$$\ln(J_s/T^2) - q^2\sigma_0^2/(2k^2T^2) = \ln(A^{**}) - q\overline{\varphi_{b0}}/(kT). \quad (9)$$

Equation (9) shows that $\ln(J_s/T^2) - q^2\sigma_0^2/(2k^2T^2)$ vs q/(kT) will be linear. The modified Richardson plot is presented in Fig. 4(c) and good linearity is observed in the whole temperature range. The calculated $\overline{\varphi_{b0}}$ is 1.05 V, in agreement with that obtained from Fig. 4(d) while A^{**} is 14.41 $A\cdot cm^{-2}\cdot K^{-2}$, very close to the theoretical data. Therefore, the temperature dependence of barrier height can be explained by BHI, which obeys the Gaussian distribution and possibly results from interface roughness. With the presence of BHI, the open circuit voltage will be much smaller than the barrier height extracted from IV curves and factors resulting in BHI should try to be avoided during HJ preparation.

In summary, $ZnSnN_2$ HJ was prepared and studied. CV curves show that the capacitance is affected by interface states and trap energy levels. The interface states form two discrete energy levels with one

14 December 2024 12:01:40

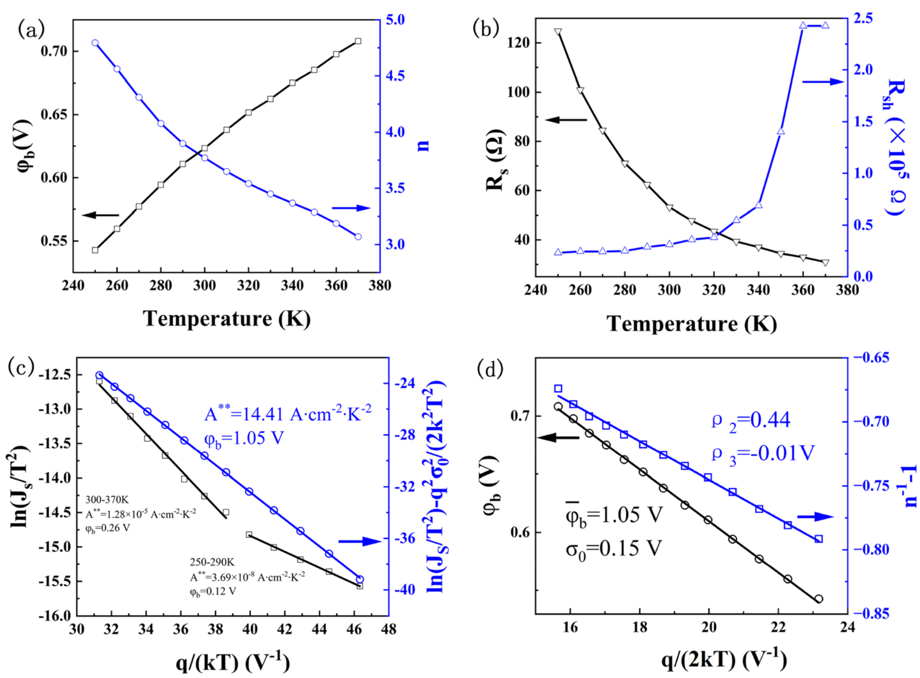

FIG. 4. (a) φ_b and n vs temperature. (b) R_s and R_{sh} vs temperature. (c) The Richardson plot and the modified one. (d) φ_b and n^{-1}–1 vs q/(2kT) plot.

Published under an exclusive license by AIP Publishing

below and one above E_c of $ZnSnN_2$. The former is also confirmed by the zero-bias difference of the charge profile. The deep energy levels are located at 0.67, 1.03 and 1.06 to 1.21 eV below E_c of $ZnSnN_2$. A shallow energy level at 105 meV below E_c is detected and the possible origin is the intrinsic antisite defect of Sn_{Zn}. JV curves show that the dominant transport mechanism is TE at lower voltage. The extracted barrier height is inhomogeneous and the possible origin is interface roughness as revealed by impedance spectra.

See the supplementary material for the following content: Methods about preparing the $Cu_2O\backslash ZnSnN_2$ heterojunctions; Characterization methods of $ZnSnN_2$ and Cu_2O; Characterizations of the photovoltaic properties of the HJ; The XRD spectra, Raman scattering spectra and Tauc plots of $ZnSnN_2$ and Cu_2O; SEM images and Hall effect measurements; The illuminated JV curve, EQE spectrum and $[E\times\ln(1-EQE)]^2$ vs E plot of the HJ; The reverse-biased C^{-2}-V curves; The fitting results based on $C = C_{SC} + C_{IS}$; The fitted C_{sc}^{-2} or $(C - C_{IS})^{-2}$ vs V curves for 100, 90, 50, 10, and 9 KHz and the calculation about the energy levels and the density; The fitting results based on Eq. (2); The C^{-2} vs V curves for 900 and 500 Hz and the calculation about the energy levels and the density; The calculation about N_{CV} and N_{DLCP}.

This work was financially supported by Natural Science Foundation of China (No. 61674107).

AUTHOR DECLARATIONS

Conflict of Interest

The authors have no conflicts to disclose.

Author Contributions

Fan Ye: Conceptualization (equal); Data curation (equal); Formal analysis (equal); Funding acquisition (equal); Investigation (equal); Methodology (equal); Project administration (equal); Resources (equal); Software (equal); Supervision (equal); Validation (equal); Visualization (equal); Writing – original draft (equal); Writing – review & editing (equal). **Zi-Cheng Zhao:** Data curation (equal); Formal analysis (equal); Investigation (equal); Methodology (equal); Software (equal); Writing – original draft (supporting). **Cang-Shuang He:** Formal analysis (supporting); Visualization (supporting). **Jian-Lin Liang:** Data curation (supporting); Formal analysis (supporting). **Qian Gao:** Data curation (supporting); Visualization (supporting). **Yi-Zhu Xie:** Resources (supporting). **Dong-Ping Zhang:** Resources (supporting). **Xing-Min Cai:** Conceptualization (equal); Data curation (equal); Formal analysis (equal); Investigation (equal); Writing – original draft (equal); Writing – review & editing (equal).

DATA AVAILABILITY

The data that support the findings of this study are available from the corresponding author upon reasonable request.

REFERENCES

[1]O. Surucu, G. Surucu, N. M. Gasanly, M. Parlak, and M. Isik, "Exploring temperature-dependent bandgap and urbach energies in CdTe thin films for optoelectronic applications," Mater. Lett. **373**, 137078 (2024).

[2]M. Isik and N. M. Gasanly, "Identification of shallow trap centers in InSe single crystals and investigation of their distribution: A thermally stimulated current spectroscopy," Opt. Mater. **156**, 116011 (2024).

[3]A. Doğan, A. Karatay, M. Isik, E. A. Yıldız, N. M. Gasanly, and A. Elmali, "Revealing the effects of defect states on the nonlinear absorption properties of the TlInSSe and $Tl_2In_2S_3Se$ crystals in near-infrared optical limiting applications," Cryst. Growth Des. **24**(17), 6981–6990 (2024).

[4]S. Y. Chen, P. Narang, H. A. Atwater, and L. W. Wang, "Phase stability and defect physics of a ternary $ZnSnN_2$ semiconductor: First principles insights," Adv. Mater. **26**(2), 311–315 (2014).

[5]J. Pan, J. Cordell, G. J. Tucker, A. C. Tamboli, A. Zakutayev, and S. Lany, "Interplay between composition, electronic structure, disorder, and doping due to dual sublattice mixing in nonequilibrium synthesis of $ZnSnN_2$: O," Adv. Mater. **31**(11), 1807406 (2019).

[6]F. Ye, C. S. He, T. Wu, S. Chen, Z. H. Su, X. H. Zhang, X. M. Cai, and G. X. Liang, "Sputtering deposited and energy band matched $ZnSnN_2$ buffer layers for highly efficient Cd-free Cu_2ZnSnS_4 solar cells," Adv. Funct. Mater. **34**(38), 2402762 (2024).

[7]Z. G. Zang, "Efficiency enhancement of ZnO/Cu_2O solar cells with well oriented and micrometer grain sized Cu_2O films," Appl. Phys. Lett. **112**(4), 042106 (2018).

[8]A. Nezhdanov, A. Skrylev, D. Shestakov, D. Usanov, D. Fukina, A. Malyshev, G. De Filpo, and A. Mashin, "Mixed phase $ZnSnN_2$ thin films for solar energy applications: Insight into optical and electrical properties," Opt. Mater. **144**, 114335 (2023).

[9]A. Laidouci, Mamta, V. N. Singh, P. K. Dakua, and D. K. Panda, "Performance evaluation of $ZnSnN_2$ solar cells with Si back surface field using SCAPS-1D: A theoretical study," Heliyon **9**(10), e20601 (2023).

[10]J. J. Cordell, S. Lany, and M. B. Tellekamp, "Comparing the influence of cation order and composition in simulated $Zn(Sn, Ge)N_2$ on structure, elastic moduli, and polarization for solid state lighting," J. Appl. Phys. **135**(7), 075001 (2024).

[11]J. W. Choi, J. Kim, S. R. Pae, J. Kim, C. G. Kim, H. Lee, S. Ji, S. W. Nam, Y. K. Lee, and B. Shin, "Oxidation-resistant amorphous zinc tin nitride films with tunable optical and electrical properties," Chem. Mater. **34**(15), 6802–6808 (2022).

[12]M. Ogura, D. Han, M. M. Pointner, L. S. Junkers, S. S. Rudel, W. Schnick, and H. Ebert, "Electronic properties of semiconducting $Zn(Si,Ge,Sn)N_2$ alloys," Phys. Rev. Mater. **5**(2), 024601 (2021).

[13]A. Laidouci, P. K. Dakua, D. K. Panda, and S. Kashyap, "Investigating the potential of earth-abundant $ZnSn_xGe_{1-x}N_2$ alloys for quantum well solar cells," Micro Nanostructures **184**, 207696 (2023).

[14]T. R. Paudel and W. R. L. Lambrecht, "First-principles study of phonons and related ground-state properties and spectra in Zn-IV-N_2 compounds," Phys. Rev. B **78**(11), 115204 (2008).

[15]L. Lahourcade, N. C. Coronel, K. T. Delaney, S. K. Shukla, N. A. Spaldin, and H. A. Atwater, "Structural and optoelectronic characterization of RF sputtered $ZnSnN_2$," Adv. Mater. **25**(18), 2562–2566 (2013).

[16]P. C. Quayle, K. L. He, J. Shan, and K. Kash, "Synthesis, lattice structure, and band gap of $ZnSnN_2$," MRS Commun. **3**(3), 135–138 (2013).

[17]K. K. Chinnakutti, V. Panneerselvam, and S. T. Salammal, "Ba-acceptor doping in $ZnSnN_2$ by reactive RF magnetron sputtering:(002) faceted Ba-$ZnSnN_2$ films," J. Alloys Compd. **855**, 157380 (2021).

[18]P. C. Quayle, E. W. Blanton, A. Punya, G. T. Junno, K. L. He, L. Han, H. P. Zhao, J. Shan, W. R. L. Lambrecht, and K. Kash, "Charge-neutral disorder and polytypes in heterovalent wurtzite-based ternary semiconductors: The importance of the octet rule," Phys. Rev. B **91**(20), 205207 (2015).

[19]B. B. Dumre, R. J. Nelson, R. E. Irving, R. J. Ellingson, and S. V. Khare, "Trends in opto-electronic properties of $Mg_xZn_{1-x}SnN_2$ using first principles methods," Mater. Chem. Phys. **294**, 126995 (2023).

[20]A. Aissat, L. Chenini, A. Laidouci, S. Nacer, and J. P. Vilcot, "Improvement in the efficiency of solar cells based on the $ZnSnN_2$/Si structure," Mater. Sci. Eng. B **300**, 117071 (2024).

[21]A. Laidouci, A. Aissat, and J. P. Vilcot, "Numerical study of solar cells based on $ZnSnN_2$ structure," Sol. Energy **211**, 237–243 (2020).

[22]M. R. Karim and H. P. Zhao, "Design of InGaN-$ZnSnN_2$ quantum wells for high-efficiency amber light emitting diodes," J. Appl. Phys. **124**(3), 034303 (2018).

14 December 2024 12:01:40

Published under an exclusive license by AIP Publishing

[23]D. Q. Fang, X. Chen, P. F. Gao, Y. Zhang, and S. L. Zhang, "Mono- and bilayer $ZnSnN_2$ sheets for visible-light photocatalysis: First-principles predictions," J. Phys. Chem. C **121**(46), 26063–26068 (2017).
[24]X. J. Wu, F. Z. Meng, D. L. Chu, M. C. Yao, K. Guan, D. D. Zhang, and J. Meng, "Carrier tuning in $ZnSnN_2$ by forming amorphous and microcrystalline phases," Inorg. Chem. **58**(13), 8480–8485 (2019).
[25]F. Ye, Z. Ke, L. H. Yuan, R. T. Hong, D. P. Zhang, P. Fan, and X. M. Cai, "Electrical and optical properties of nanocrystalline $ZnSnN_2$," Thin Solid Films **772**, 139804 (2023).
[26]A. N. Fioretti, A. Stokes, M. R. Young, B. Gorman, E. S. Toberer, A. C. Tamboli, and A. Zakutayev, "Effects of hydrogen on acceptor activation in ternary nitride semiconductors," Adv. Electron. Mater. **3**(3), 1600544 (2017).
[27]F. Ye, Q. Q. Chen, X. M. Cai, Y. Z. Xie, X. F. Ma, K. Vaithinathan, D. P. Zhang, P. Fan, and V. A. L. Roy, "Improving the chemical potential of nitrogen to tune the electron density and mobility of $ZnSnN_2$," J. Mater. Chem. C **8**(13), 4314–4320 (2020).
[28]J. Y. Ren, L. Y. Liang, X. H. Liu, and H. T. Cao, "Physical properties of Zn-Sn-N films governed by the Zn/(Zn+Sn) ratio," J. Vac. Sci. Technol. A **41**(3), 033406 (2023).
[29]F. Ye, R. T. Hong, C. S. He, Z. C. Zhao, Y. Z. Xie, D. P. Zhang, F. Wang, J. W. Li, and X. M. Cai, "$ZnSnN_2$ Schottky barrier solar cells," Mater. Sci. Eng. B **300**, 117097 (2024).
[30]R. F. Qin, H. T. Cao, L. Y. Liang, Y. F. Xie, F. Zhuge, H. L. Zhang, J. H. Gao, K. Javaid, C. C. Liu, and W. Z. Sun, "Semiconducting $ZnSnN_2$ thin films for Si/$ZnSnN_2$ p-n junctions," Appl. Phys. Lett. **108**(14), 142104 (2016).
[31]K. Javaid, W. H. Wu, J. Wang, J. F. Fang, H. L. Zhang, J. H. Gao, F. Zhuge, L. Y. Liang, and H. T. Cao, "Band offset engineering in $ZnSnN_2$-based heterojunction for low-cost solar cells," ACS Photonics **5**(6), 2094–2099 (2018).
[32]F. Ye, R. T. Hong, Y. B. Qiu, Y. Z. Xie, D. P. Zhang, P. Fan, and X. M. Cai, "Nanocrystalline $ZnSnN_2$ prepared by reactive sputtering, its Schottky diodes and heterojunction solar cells," Nanomaterials **13**(1), 178 (2022).
[33]B. K. Meyer, A. Polity, D. Reppin, M. Becker, P. Hering, P. J. Klar, T. Sander, C. Reindl, J. Benz, M. Eickhoff, C. Heiliger, M. Heinemann, J. Bläsing, A. Krost, S. Shokovets, C. Müller, and C. Ronning, "Binary copper oxide semiconductors: From materials towards devices," Phys. Status Solidi B **249**(8), 1487–1509 (2012).
[34]R. C. Wang and C. H. Li, "Cu, Cu-Cu_2O core-shell, and hollow Cu_2O nanodendrites: Structural evolution and reverse surface-enhanced Raman scattering," Acta Mater. **59**(2), 822–829 (2011).
[35]Y. S. Lee, M. T. Winkler, S. C. Siah, R. Brandt, and T. Buonassisi, "Hall mobility of cuprous oxide thin films deposited by reactive direct-current magnetron sputtering," Appl. Phys. Lett. **98**(19), 192115 (2011).
[36]A. El-Shaer, N. Darwesh, M. A. Habib, and M. Abdelfatah, "Doping of nanostructured Cu_2O films to improve physical and photoelectrochemical properties as a step forward for optoelectronics applications," Opt. Mater. **148**, 114849 (2024).
[37]A. Lakshmanan, Z. C. Alex, and S. R. Meher, "N-type In (or Al) doped Cu_2O thin films by magnetron sputtering," Eur. Phys. J. Plus **139**, 62 (2024).
[38]P. K. Vasudev, B. L. Mattes, E. Pietras, and R. H. Bube, "Excess capacitance and non-ideal Schottky barriers on GaAs," Solid-State Electron. **19**(7), 557–559 (1976).
[39]A. M. Goodman, "Metal-semiconductor barrier height measurement by the differential capacitance method-one carrier system," J. Appl. Phys. **34**(2), 329–338 (1963).
[40]G. I. Roberts and C. R. Crowell, "Capacitance energy level spectroscopy of deep-lying semiconductor impurities using Schottky barriers," J. Appl. Phys. **41**(4), 1767–1776 (1970).
[41]G. I. Roberts and C. R. Crowell, "Capacitive effects of Au and Cu impurity levels in Pt-n type Si Schottky barriers," Solid-State Electron. **16**(1), 29–38 (1973).
[42]E. H. Nicollian and A. Goetzberger, "The Si-SiO_2 interface-electrical properties as determined by the metal-insulator silicon conductance technique," Bell Syst. Tech. J. **46**(6), 1055–1133 (1967).
[43]D. G. Zhao, D. S. Jiang, J. J. Zhu, Z. S. Liu, H. Wang, S. M. Zhang, Y. T. Wang, and H. Yang, "Role of edge dislocation and Si impurity in linking the blue luminescence and yellow luminescence in n-type GaN films," Appl. Phys. Lett. **95**(4), 041901 (2009).
[44]A. D. Prins, M. K. Lewis, Z. L. Bushell, S. J. Sweeney, S. Liu, and Y.-H. Zhang, "Evidence for a defect level above the conduction band edge of InAs/InAsSb type-II superlattices for applications in efficient infrared photodetectors," Appl. Phys. Lett. **106**(17), 171111 (2015).
[45]W. R. Anderson, R. G. Wheeler, and T. P. Ma, "Observation of interface traps in the silicon conduction band at the (100)Si/SiO_2 interface at 4.2 K," Appl. Phys. Lett. **61**(9), 1107–1109 (1992).
[46]P. Cova and A. Singh, "Temperature dependence of I-V and C-V characteristics of Ni/n-CdF_2 Schottky barrier type diodes," Solid-State Electron. **33**(1), 11–19 (1990).
[47]I. Balberg, "Relation between distribution of states and the space-charge-region capacitance in semiconductors," J. Appl. Phys. **58**(7), 2603–2616 (1985).
[48]J. T. Heath, J. D. Cohen, and W. N. Shafarman, "Bulk and metastable defects in $CuIn_{1-x}Ga_xSe_2$ thin films using drive-level capacitance profiling," J. Appl. Phys. **95**(3), 1000–1010 (2004).
[49]T. Walter, R. Herberholz, C. Müller, and H. W. Schock, "Determination of defect distributions from admittance measurements and application to Cu(In, Ga)Se_2 based heterojunctions," J. Appl. Phys. **80**(8), 4411–4420 (1996).
[50]S. Chand and J. Kumar, "Current-voltage characteristics and barrier parameters of Pd_2Si/p- Si(111) Schottky diodes in a wide temperature range," Semicond. Sci. Technol. **10**, 1680 (1995).
[51]L. F. Marsal, I. Martin, J. Pallares, A. Orpella, and R. Alcubilla, "Annealing effects on the conduction mechanisms of p^+- amorphous- $Si_{0.8}C_{0.2}$: H/n- crystalline- Si diodes," J. Appl. Phys. **94**(4), 2622–2626 (2003).
[52]T. F. Schulze, L. Korte, E. Conrad, M. Schmidt, and B. Rech, "Electrical transport mechanisms in a-Si:H/c-Si heterojunction solar cells," J. Appl. Phys. **107**(2), 023711 (2010).
[53]E. Arslan, Ş. Altındal, S. Özçelik, and E. Ozbay, "Dislocation-governed current-transport mechanism in (Ni/Au)- AlGaN/AlN/GaN heterostructures," J. Appl. Phys. **105**(2), 023705 (2009).
[54]J. H. Werner and H. H. Güttler, "Barrier inhomogeneities at Schottky contacts," J. Appl. Phys. **69**(3), 1522–1533 (1991).
[55]J. H. Werner and H. H. Güttler, "Transport properties of inhomogeneous Schottky contacts," Phys. Scr. **T39**, 258–264 (1991).
[56]M. Isik, O. Surucu, and N. M. Gasanly, "Temperature-dependent current-voltage characteristics of p- $GaSe_{0.75}S_{0.25}$/n- Si heterojunction," Appl. Phys. A **129**(8), 538 (2023).

14 December 2024 12:01:40

Published under an exclusive license by AIP Publishing